Numerical Modeling of a Line of Towering Cumulus on Day 226 of GATE

FRANK B. LIPPS AND RICHARD S. HEMLER

Geophysical Fluid Dynamics Laboratory/NOAA, Princeton University, Princeton, New Jersey

(Manuscript received 30 December 1986, in final form 3 March 1988)

ABSTRACT

A three-dimensional numerical model with warm rain bulk cloud physics is used to investigate the shallow convection observed on day 226 of GATE. This convection had cloud tops at 3.0 km, cloud bases at 0.4 km and approximately 0.1 cm of rain at the surface. The simulated convection shows a strong sensitivity to the criterion for the onset of autoconversion of cloud water into rain water. The strongest convection occurs for the case in which no rain water forms. This case, however, does not conform to the observed convection, lacking the downdraft below cloud base and the observed strong surface outflow.

The primary simulation produces a "finger" of convection propagating to the northeast, perpendicular to the northwest–southeast orientation of the larger-scale line of convection. The orientation and propagation speed of the calculated convection are in excellent agreement with observed radar data. This simulation also has a well-defined leading edge and strong surface outflow as observed. In poorer agreement, the cloud base was too high and the rainfall at the surface was less than observed.

Present calculations indicate that the boundary layer air is flowing through the line from southwest to northeast below cloud base. The primary moisture source for the cloud is the upper half of the subcloud layer, with nearly horizontal flow entering the cloud.

1. Introduction

In this study numerical calculations are performed to simulate the shallow convection observed on day 226 (14 August 1974) of the Global Atmospheric Research Program (GARP) Atlantic Tropical Experiment (GATE). As reported by Pennell (1975), a line of towering cumulus with cloud tops near 3.0 km was oriented in a northwest to southeast direction and ran from the ship *Oceanographer* to the ship *Gillis* and beyond. When this project was initiated, it was intended that this case study would be used to examine the sensitivity of the present numerical model to initial conditions. Our planning was guided by the suggestion of the WMO Weather Modification Research Programme (1986) which indicated that good boundary layer data were available so that this case would be appropriate to study the importance of initial conditions in modeling convection.

After examining the observational data for this case study in detail, however, we realized that our first priority had to be to investigate the dynamics of this type of convection; shallow convection appears deceptively simple. One of the authors (Lipps 1977) attempted to simulate an observed case of quasi-steady shallow convection in the Caribbean (Malkus 1954). In that study, a single cell, forced by the initial disturbance, formed and decayed. The same result has been obtained in later unpublished calculations in which the original periodic lateral boundary conditions were replaced by more realistic open lateral conditions. Thus, a primary goal of the present study is to simulate the successive formation of new cells just behind the leading (northeastern) edge of the line, as is inferred to be the nature of the observed data (Pennell 1975). The detailed discussion of the calculations performed in this study indicates that we have been successful in this goal.

The present numerical model with warm rain bulk cloud physics is described in section 2. Additional details of the subgrid-scale turbulence parameterization are given in the Appendix. In section 3 the base state and initial conditions are described, while in section 4, the set of eight calculations are discussed in detail. The sensitivity of the present simulations to the criterion for the onset of autoconversion of cloud water into rain water is presented in section 5. A detailed comparison is made between the primary calculation, run B_2, and the calculation with no rain water, run B_3. The remaining calculations are described in section 6. A comparison with observations is given in section 7. It is seen that the convection in run B_2 forms a "finger" of convection normal to the larger-scale line discussed by Pennell. The orientation and propagation speed to the northeast of this small-scale feature are in excellent agreement with the radar data shown in Fig. 14. Finally, a summary of the present study is given in section 8.

Corresponding author address: Dr. Frank B. Lipps, NOAA/Geophysical Fluid Dynamics Laboratory, Princeton University, Princeton, NJ 08542.

2. The moist convection model

The basic properties of the numerical model are described in Lipps and Hemler (1986) and in the earlier scale-analysis study of Lipps and Hemler (1982). These studies are hereafter referred to as LH86 and LH82, respectively. The present set of equations are the deep anelastic system using Cartesian (x, y, z)-coordinates as given in LH86.

In these equations, the atmospheric pressure p is represented through the Exner pressure function π which is defined by

$$\pi = (p/P)^{\kappa}, \quad \kappa = R_d/c_p \tag{2.1}$$

where P (=1000 mb) is a reference pressure, R_d (=287.04 J kg^{-1} K^{-1}) is the gas constant and c_p (=1005.7 J kg^{-1} K^{-1}) is the specific heat at constant pressure for dry air. The relation $T = \pi\theta$ between the temperature T and the potential temperature θ is obtained from the definition of θ. For the present calculations, the mean surface pressure is 1015 mb. Thus, using $T = \pi\theta$, it is seen that surface values of θ are slightly smaller than the corresponding values of T.

The saturation water vapor mixing ratio q_{vs} is given by

$$q_{vs} = \frac{\epsilon e_s}{p_0 - e_s} \tag{2.2}$$

where $p_0(z)$ is the base state pressure, e_s the saturation vapor pressure, $\epsilon = R_d/R_v$ and R_v (=461.50 J kg^{-1} K^{-1}) is the gas constant for water vapor. This form of q_{vs} is more accurate than often used in cloud modeling as it includes the term $-e_s$ in the denominator (see LH82).

The thermodynamic variables are separated into the components

$$\begin{aligned} \theta &= \theta_0(z) + \theta_1(x, y, z, t) \\ \pi &= \pi_0(z) + \pi_1(x, y, z, t) \\ T &= T_0(z) + T_1(x, y, z, t) \end{aligned} \tag{2.3}$$

where θ_0, π_0 and T_0 are associated with the hydrostatic base state, and θ_1, π_1 and T_1 are due to the convection. Since the latter variables are at least an order of magnitude smaller than the base state variables, the relation $T = \pi\theta$ can be represented by $T_0 = \pi_0\theta_0$ for the base state. Thus, if $T_0(z)$ is known from observations, then π_0 and θ_0 can be calculated from the hydrostatic equation and the relation $T_0 = \pi_0\theta_0$. Finally, using the equation of state for dry air, the base state density $\rho_0(z)$ can be obtained from the known values of $T_0(z)$ and $\pi_0(z)$.

a. *The equations of motion*

1) CONTINUITY AND MOMENTUM

The equations of motion are written in tensor notation with the vector velocity (u, v, w) being denoted by u_i. For the anelastic set of equations (Ogura and Phillips 1962) continuity is represented by

$$\frac{\partial}{\partial x_j}(\rho_0 u_j) = 0. \tag{2.4}$$

The momentum equation in tensor form is given by

$$\begin{aligned} \frac{\partial}{\partial t}(\rho_0 u_i) + \frac{\partial}{\partial x_j}(\rho_0 u_i u_j) &= -\rho_0 \frac{\partial \phi}{\partial x_i} - D_i \\ &+ \delta_{i3}\rho_0 g\left(\frac{\theta_1}{\theta_0} + 0.608 q_v - q_c - q_r\right) + \frac{\partial \tau_{ij}}{\partial x_j} \end{aligned} \tag{2.5}$$

where g (=9.781 m s^{-2}) is the acceleration due to gravity and τ_{ij} is the subgrid-scale Reynolds stress tensor. The subgrid-scale turbulence parameterization is given in the Appendix. In the present scheme, vertical mixing is greatly reduced in regions with stable stratification both in cloud and in clear air. This is a generalization of the scheme outlined in LH86. The new scheme also allows reasonable values of mixing to occur even when the grid intervals Δx, Δy and Δz differ significantly in size. In the present calculations Δx and Δy are a factor of 4 larger than Δz.

The variable ϕ is defined as in LH82

$$\phi = c_p\theta_0\pi_1. \tag{2.6}$$

Since the present equations are anelastic, ϕ is calculated from a Poisson equation which is obtained by taking the divergence of (2.5).

Finally, the term D_i represents a Newtonian damping which maintains the initial base state fields $U(z)$ and $V(z)$ from being significantly degraded by unrealistic diffusion effects. In the present model, such effects occur primarily in the surface boundary layer as will be discussed in section 6. This term is given by

$$-D_i = \rho_0 a\{(U - \langle u\rangle)\delta_{i1} + (V - \langle v\rangle)\delta_{i2}\} \tag{2.7}$$

where $a = 10^{-3}$ sec^{-1} and the angle brackets denote a horizontal average. A comparison of calculations with and without this term will be made in section 6.

2) THERMODYNAMICS AND MOISTURE

The thermodynamic equation is given by

$$\begin{aligned} \frac{\partial}{\partial t}(\rho_0\theta_1) + \frac{\partial}{\partial x_j}[\rho_0 u_j(\theta_0 + \theta_1 - \theta_{00})] \\ = \frac{\rho_0 L}{c_p\pi_0}(C_d - E) - \frac{\partial}{\partial x_j}(\rho_0\overline{u_j'\theta'}) \end{aligned} \tag{2.8}$$

where $\rho_0\overline{u_j'\theta'}$ are the subgrid-scale fluxes associated with θ. The form of $\rho_0\overline{u_j'\theta'}$ as well as the corresponding moisture fluxes are also discussed in the Appendix. Here, C_d is the condensation/evaporation of cloud water q_c and E is the evaporation of rain water q_r; L (=0.2454 × 10^7 J kg^{-1}) is the latent heat of vaporization and θ_{00} (=308.47 K) is the mean of θ_0 at the surface

and the model upper boundary. This parameter is included in (2.8) to improve the accuracy of the numerical integration.

The value of L is chosen to correspond to the value of the latent heat of vaporization at 20°C. This temperature in the base state occurs at $z = 750$ m and is located in the lower cloud levels in the model simulation. The values of C_d are determined by requiring $q_v = q_{vs}$ whenever cloud water q_c is present. The method for calculating C_d is given in appendix A of LH82.

Unlike the calculations in LH86, spurious gravity waves due to reflection were not evident near the upper boundary. Since this boundary is at $z = 4.5$ km in the present model, the moderate values of static stability near this level apparently did not allow significant energy to accumulate in these waves. Thus, no Newtonian damping term was required in (2.8).

The present warm rain bulk cloud physics follows Kessler (1969) for which cloud water q_c moves with the air and the rain water q_r has the fall velocity $-V_T$ relative to the air. Thus the equations governing moisture conservation are given by

$$\frac{\partial}{\partial t}(\rho_0 q_v) + \frac{\partial}{\partial x_j}(\rho_0 u_j q_v) = -\rho_0(C_d - E) - \frac{\partial}{\partial x_j}(\rho_0 \overline{u_j' q_v'}) \quad (2.9)$$

$$\frac{\partial}{\partial t}(\rho_0 q_c) + \frac{\partial}{\partial x_j}(\rho_0 u_j q_c) = \rho_0(C_d - S_a - S_c) - \frac{\partial}{\partial x_j}(\rho_0 \overline{u_j' q_c'}) \quad (2.10)$$

$$\frac{\partial}{\partial t}(\rho_0 q_r) + \frac{\partial}{\partial x_j}(\rho_0 u_j q_r) - \frac{\partial}{\partial z}(\rho_0 V_T q_r) = \rho_0(S_a + S_c - E) - \frac{\partial}{\partial x_j}(\rho_0 \overline{u_j' q_r'}) \quad (2.11)$$

where S_a is the autoconversion of q_c into q_r, S_c is collection of q_c by falling raindrops, and $\rho_0 \overline{u_j' q_v'}$, $\rho_0 \overline{u_j' q_c'}$ and $\rho_0 \overline{u_j' q_r'}$ are the subgrid-scale fluxes.

The detailed bulk cloud physics is a modified version of the formulation presented by Manton and Cotton (1977). The expression for the autoconversion S_a is given by

$$S_a = 7.00 \times 10^{-7} \rho_0^{4/3} q_c^{7/3} h(q_c - q_{cm}) \quad (2.12)$$

where $h(x)$ is the Heaviside unit step function and q_{cm} is the minimum value of q_c below which there is no autoconversion. In this equation, ρ_0 and q_c have the units of kg m^{-3} and g kg^{-1} respectively. Equation (2.12) for S_a is discussed in detail since numerical calculations are carried out with three different values of $\rho_0 q_{cm}$. Expressions for S_c, V_T and E are given in the appendix of LH86.

b. Numerical methods

The numerical procedure for the present model follows that described in LH82 and LH86. Grid points for u, v, w and ϕ are staggered in space with the Poisson equation for ϕ being solved at ϕ-grid points. For the present calculations, the grid intervals are $\Delta x = \Delta y = 250$ m and $\Delta z = 62.5$ m. With this vertical resolution, horizontal velocities and thermodynamic variables are evaluated at $z = 31.25$ m and $z = 156.25$ m, which are virtually identical with the two levels where flight data were obtained by Pennell (1975). At the beginning of the calculations the time step was $\Delta t = 10$ sec. For strong convection, where $w > 4$ m s^{-1}, Δt had to be reduced to 5 s.

The momentum equation (2.5) is solved using centered space and time differences as discussed in LH82. The prognostic equations (2.9)–(2.11) for q_v, q_c and q_r are solved using the method described by Clark (1979). The motivation for using this scheme is to eliminate the problem of numerically generated spurious negative values of q_v, q_c and q_r. As discussed by Clark (1979), away from regions where such values are likely, the present method is very close to the unmodified Crowley (1968) scheme.

The prognostic equation (2.8) for θ_l is solved by using the second order Crowley scheme. This method of solution of (2.8) is consistent with the solution of the prognostic equation for q_v and thus allows an efficient numerical algorithm for calculating the condensation/evaporation C_d of cloud water.

c. Boundary conditions

The moist model has the capability of applying either open or periodic conditions at lateral boundaries. For open lateral boundaries, the present scheme for specifying the normal velocity is a slightly modified form of the Orlanski (1976) condition. For the other variables evaluated at open boundaries, simple specification at inflow boundaries and extrapolation at outflow boundaries produces satisfactory results (Klemp and Wilhelmson 1978; Clark 1979). As indicated in section 3, the simulations in this study have open conditions at lateral boundaries in x and either open or periodic conditions for lateral boundaries in y.

Rigid boundaries are assumed at the surface ($z = 0$) and model top ($z = 4.5$ km) so that $w = 0$ there. Due to the staggered grid used in the present model, the variables u, v, θ, q_v, q_c and q_r are evaluated at a one-half grid interval (31.25 m) from the upper boundary. At this level, the vertical gradients of the corresponding vertical subgrid-scale fluxes are required to vanish as in Klemp and Wilhelmson (1978). At the surface, vertical derivatives of q_c and q_r are required to vanish and a drag law formulation is used to specify $\rho_0 \overline{u'w'}$, $\rho_0 \overline{v'w'}$, $\rho_0 \overline{w'\theta'}$ and $\rho_0 \overline{w'q_v'}$. This formulation follows that given in LH86.

3. Initial conditions

For the present calculations, the positive x-axis is rotated 68.2 deg toward the north from the usual direction of due east. (Thus the x-axis is oriented from SSW to NNE.) This direction was chosen to correspond to the flight paths taken to obtain the boundary layer data discussed in Pennell (1975).

The soundings for the base state potential temperature θ_0 and water vapor mixing ratio q_v are shown in Fig. 1a. These soundings were obtained using two steps. First, the data from the ship *Gillis* at 1200 and 1500 UTC were averaged to obtain a sounding representative of 1330 UTC. These mean soundings appear to be compatible with the flight data available at higher levels. Secondly, the lower level data were adjusted to be compatible with the flight data of Pennell (1975) at z = 30.5 and 152.4 m. The moisture profile, however, has larger values than indicated by the flight data and thus corresponds more closely with the *Gillis* data. The dashed line indicates a 5% moisture augmentation from z = 0.7 to 2.0 km. This vertical layer corresponds to lower and midlevels of the observed clouds.

The base state horizontal velocities U and V were also obtained as a mean of the 1200 and 1500 UTC *Gillis* data. The mean winds, thus calculated, had to be rotated by 68.2 deg to give the U and V velocities shown in Fig. 1b which are compatible with the present (x, y)-coordinates. Boundary layer values were also modified to be compatible with the flight data. Note that in the present coordinate system V has very small values between z = 1.5 km and the surface.

The curve labeled θ_{moist} in Fig. 1a is obtained from a pseudomoist-adiabatic parcel calculation where the assumed cloud base at z = 594 m is at the same temperature as the environment. This calculation is carried out as described in Lipps and Hemler (1980). A comparison of the θ_0 and θ_{moist} curves indicates strong moist instability, and some cells of deep moist convection were observed on day 226 of GATE. As shown in Fig.

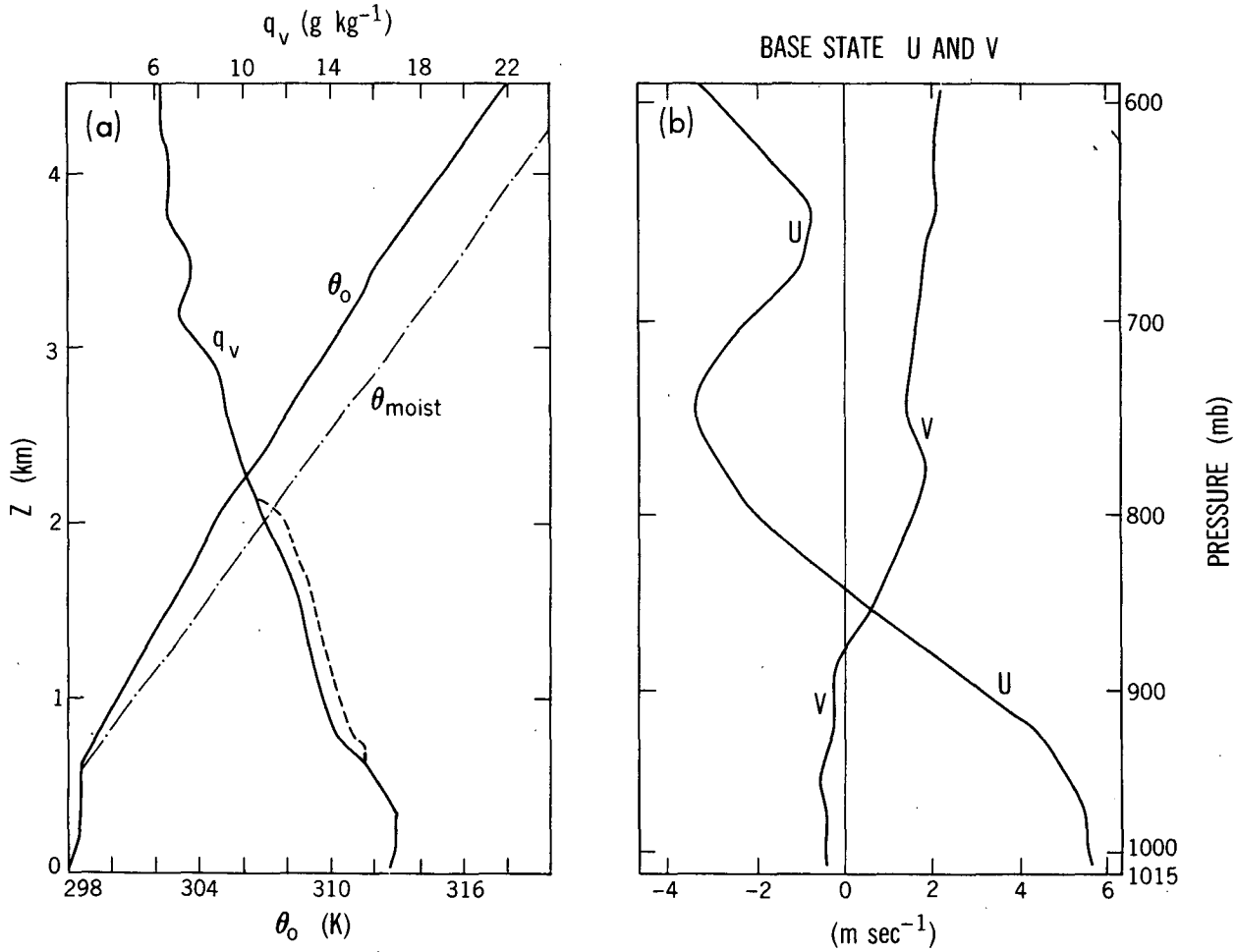

FIG. 1. Base state soundings with height. (a) The base state potential temperature θ_0 and water vapor mixing ratio q_v. Short dashed line indicates 5% moisture augmentation. Dash–dot line indicates a pseudomoist-adiabatic parcel calculation. (b) Vertical profiles of base state horizontal velocities U and V.

1b, strong vertical wind shear was present within the cloud layers. This vertical wind shear along with a relatively dry layer just above 3 km (Fig. 1a) evidently acted together to inhibit the further growth of the observed shallow convection.

The convection was initiated by a moisture disturbance at time $t = 0$ given by

$$q_v' = q_0 \exp\{-\alpha[(x - x_0)^2 + (y - y_0)^2 + 16(z - z_0)^2]\} \quad (3.1)$$

where $q_0 = 1.0$ g kg^{-1}, $\alpha = 1.28 \times 10^{-6}$ m^{-2} and $z_0 = 656.25$ m. The values of x_0 and y_0 depend on the particular calculation considered. The disturbance q_v' is set to zero outside the region defined by

$$\begin{aligned} -10^3 \text{ m} &\leqslant x - x_0 \leqslant 10^3 \text{ m} \\ -10^3 \text{ m} &\leqslant y - y_0 \leqslant 10^3 \text{ m} \\ -375 \text{ m} &\leqslant z - z_0 \leqslant 375 \text{ m} \end{aligned} \quad (3.2)$$

The center of the q_v' disturbance located at (x_0, y_0, z_0) has a value of the total q_v which is only slightly subsaturated.

4. Set of calculations

In the present investigation a set of eight calculations are carried out. The salient features of these calculations are summarized in Table 1. For all cases the origin of the Cartesian coordinates is at the surface and in the center of the horizontal domain. Also, in order to maintain the convection near the center of the horizontal domain, the coordinate system is required to translate at 4 m s^{-1} in the positive x-direction toward the NNE. Unless stated otherwise, all calculations use open lateral boundary conditions in both x and y, and the base state profile of q_v in Fig. 1a has the 5% moisture augmentation included between $z = 0.7$ and 2.0 km. Equation (2.12) indicates that $q_c \geqslant q_{cm}$ is necessary for the start of autoconversion of cloud water into rain water. As shown in Table 1, $\rho_0 q_{cm} = 1.0$ g m^{-3} for most of the calculations.

TABLE 1. Set of calculations in the present study. See text for detailed discussion of the different runs.

Run	$\rho_0 q_{cm}$ (g m^{-3})	Lateral B.C.	Comments
A_1	1.0	Open (x)	Two-dimensional
A_2	1.0	Open (y)	Two-dimensional
B_1	0.5	Open (x, y)	
B_2	1.0	Open (x, y)	
B_3	∞	Open (x, y)	
C_1	1.0	Open (x, y)	$a = 0$ in Eq. (2.7)
C_2	1.0	Open (x, y)	No moisture augmentation in base state
C_3	1.0	Open (x) Periodic (y)	4 km width in y

The data in Fig. 1b indicate that a strong vertical wind shear is present in U throughout the lower and middle levels of the observed clouds. For this reason, the primary emphasis is placed upon three-dimensional simulations, with run B_2 being taken as the standard calculation against which the other calculations are compared. For calculations B_1, B_2 and B_3, the value of $\rho_0 q_{cm}$ is varied as indicated in Table 1. For these three simulations, the horizontal domain is 10 km long in x and 6 km wide in y. In addition, the center of the q_v' disturbance at $t = 0$ is located at $x_0 = -2.625$ km and $y_0 = 0.375$ km.

The two-dimensional calculations A_1 and A_2 are carried out to compare the properties of roll-type convection oriented perpendicular to and parallel with the x-axis. In run A_1, with the roll axis perpendicular to the x-axis, the $(y - y_0)^2$ term is dropped from (3.1) and $x_0 = -2.625$ km. In run A_2, with the roll axis parallel with the x-axis, the $(x - x_0)^2$ term is dropped from (3.1) and $y_0 = -2.625$ km. For both calculations the channel length is 20 km.

In the simulation C_1, the Newtonian-type term D_i has been dropped from the momentum equation (2.5). This is equivalent to setting the coefficient $a = 0$ in Eq. (2.7) which specifies $-D_i$. In all other respects run C_1 is similar to run B_2. Run C_2 is the same as run B_2 except that the moisture augmentation, shown as the dashed line in Fig. 1a, is not included in this calculation. Finally, run C_3 is similar to run B_2 except that periodic lateral boundary conditions are applied in y. The purpose of this calculation was to simulate a line of convection oriented from NW to SE as reported by Pennell (1975). The width of the horizontal domain in y is 4 km for run C_3. In all other three-dimensional simulations, the width is 6 km in y.

5. Role of the onset value for autoconversion

a. Comparison of runs B_1, B_2 and B_3

The calculations carried out in the present study indicate that the simulated shallow convection is sensitive to the value of $\rho_0 q_{cm}$, which is the onset value for the start of autoconversion of cloud water into rain water. Thus, in this section we compare the three-dimensional calculations B_1, B_2 and B_3 for which $\rho_0 q_{cm}$ is varied as indicated in Table 1. In section 5b, more detailed features of the convection will be shown for runs B_2 and B_3.

The maximum vertical velocity w_{max} as a function of time is shown in Fig. 2 for these three calculations. For all three cases, the first maximum in w_{max} occurs at 20 min after the start of the computations. This first peak is obviously associated with the initial disturbance q_v' given by Eq. (3.1). The following variations of w_{max} with time, however, appear to be governed by the dynamics of the convection.

In runs B_1 and B_2, the convection changes profoundly after 100 min. Before this time, the convection

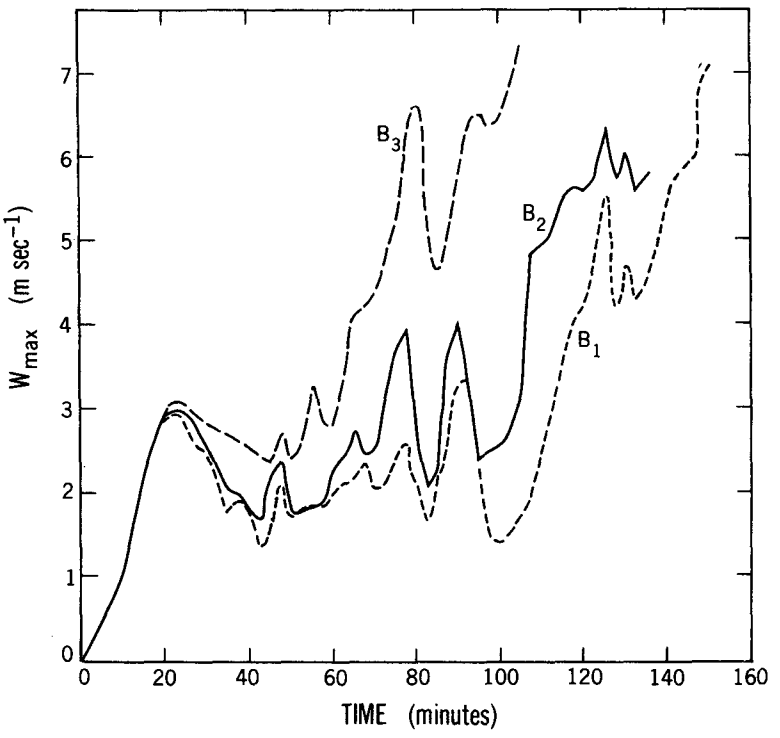

FIG. 2. Plot of maximum vertical velocity w_{max} with time. Solid line, run B_2; short-dashed line, run B_1; long-dashed line, run B_3.

is shallow with cloud tops no higher than 3 km and values of w_{max} no larger than 4 m s^{-1}. The convection does not die out after the initial peak in w_{max} at 20 min: rather, a well-defined leading edge remains relatively stationary in space with turrets forming just behind the leading edge and advecting out the negative x-boundary. Rainfall from these cells is no more than 0.02 cm at the ground. After 100 min, deep cells start forming which reach the upper boundary in both runs B_1 and B_2. Although the simulation of these cells is beyond the scope of the present investigation, observations indicate that scattered deep cells were present on day 226 of GATE. Some of these deep cells are indicated in the radar data shown in Fig. 14 at 15 UTC.

The data in Fig. 2 indicate that run B_3, with $\rho_0 q_{cm} = \infty$ (no rain water), develops more vigorously than the other two cases. The convection is also weaker for run B_1 than for run B_2. Thus the autoconversion of cloud water q_c into rain water q_r weakens the convection in the present simulations. In order to clarify this result, the horizontal average vertical velocity $\langle w \rangle$ is plotted as a function of z in Fig. 3 for these three calculations at 80 min. The heavy dashed line represents the cloud base at $z = 562$ m. As shown in this figure, mean sinking occurs below cloud base for runs B_1 and B_2, whereas in run B_3, mean rising motion occurs there. From the

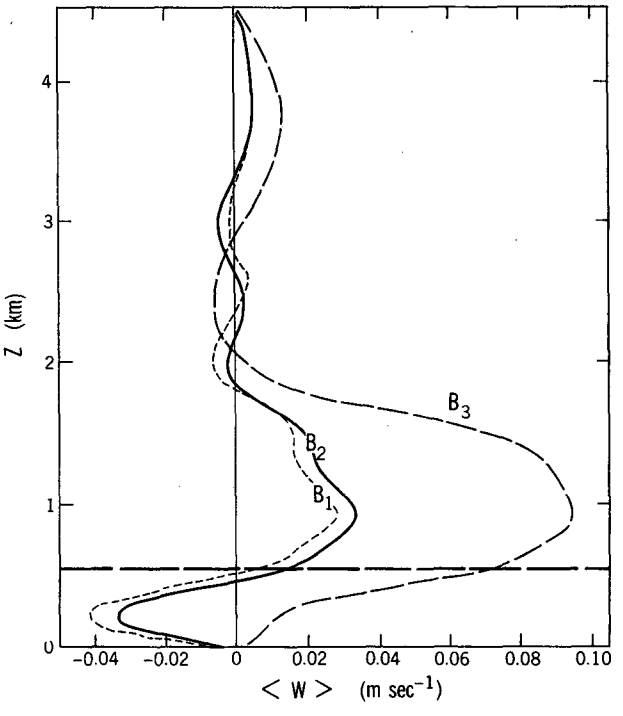

FIG. 3. Plot of horizontal average vertical velocity $\langle w \rangle$ as a function of z at 80 min. Solid line, run B_2; short-dashed line, run B_1; long-dashed line, run B_3. Heavy dashed line is cloud base.

vertical profiles of $\langle w \rangle$, it appears that runs B_1 and B_2 have much more in common with each other than they have with run B_3.

The discussion in section 5b will show that the sinking motion below cloud base inhibits low-level moisture from entering the cloud in Run B_2. This sinking motion is associated with the presence of rain water and evaporative cooling. With mean rising motion below cloud base in run B_3, it could be anticipated that the convection is stronger in this calculation. The stronger convection in run B_3 is also borne out by the large values of $\langle w \rangle$ near and above cloud base. It will be seen in section 5b, however, that run B_2 is much more consistent with the surface observations of Pennell (1975).

b. *Discussion of runs B_2 and B_3*

1) RUN B_2

Horizontal cross sections at 80 min for run B_2 at $z = 1.906$ km are shown in Fig. 4. Three cells in w are present with significant rain water only associated with the cell near the x-boundary. This rain water fell from a region with strong vertical velocity at higher levels. Note that the three cells and the area with cloud water are oriented generally in a line at 15 deg to the present x-axis. Since the positive x-axis is toward the NNE, this line is oriented NE–SW.

Due to the slant of the convection with respect to the x-axis, it is not possible to obtain one x–z cross

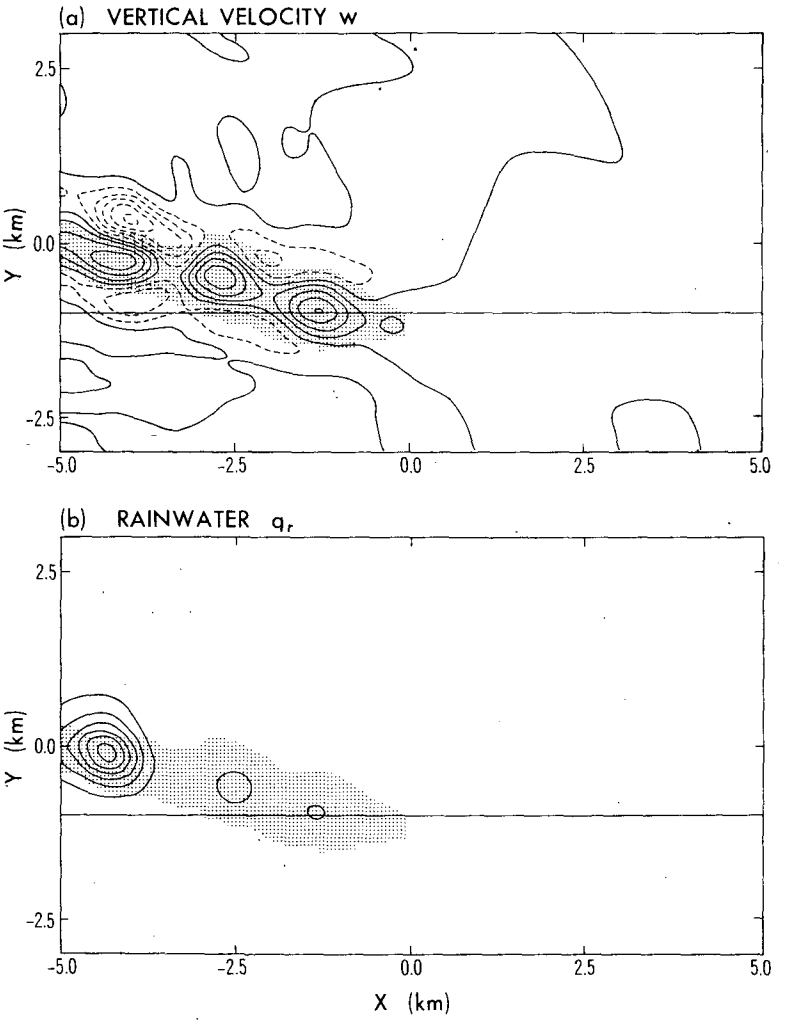

FIG. 4. Horizontal cross sections at 80 min for run B_2 at $z = 1.906$ km. (a) Vertical velocity with $w_{max} = 1.15$ m s^{-1} and $w_{min} = -1.43$ m s^{-1}. (b) Rain water q_r. Maximum value is 0.10 g kg^{-1}. Stippled areas represent cloud. Dashed lines indicate negative values. Solid line at $y = -1.125$ km indicates intersection with Fig. 5.

section representative of all three cells in Fig. 4. The cross sections plotted in Fig. 5 at $y = -1.125$ km intersect the leading cell and the leading edge of the line in Fig. 4. In Fig. 5, however, this cell turns out to be the second, and deeper, convective element. The data in this figure also indicate a well-defined leading edge of the convection with vertical velocity "roots" extending somewhat below cloud base for both primary convective elements. From both of these figures, it is seen that the cloud layer slants upward and toward larger values of y. Thus, the convection in run B_2 is made up of turrets which form just behind the leading edge and then move SW along the line. Figure 5 also indicates that sinking motion and cool temperatures are present below cloud base.

In Fig. 6, cross sections are again plotted at $y = -1.125$ km to show the rain water q_r and the vector velocity field in the x–z plane at 80 min. Note that the vertical scale is twice the horizontal in this figure. The most important feature shown is the branching of the flow field below cloud base with the weaker branch moving horizontally into the slanting cloud base and the stronger branch descending toward the surface. Near and ahead of the leading cloud edge, the model winds are stronger at the surface than at 30 m. This result and the well-defined leading edge of the convection are in agreement with the discussion of Pennell (1975).

At this point we examine the orientation and motion of the present line of convection. The orientation of the line was determined from the cloud water q_c pattern at $z = 1.906$ km at 80 min. This field has an appearance very similar to the w-field shown in Fig. 4a. The orientation of the primary cells form a line at an angle of 15.1 deg to the right of the present x-axis. Thus the line of convection has an angle of 36.9 deg with respect to North.

The movement of the line was determined from the speed of the leading edge of the 10^{-2} cm accumulated rain at the ground. This means of calculating the motion of the line seems consistent for comparison with the observed radar data discussed in section 7. We found that the line in run B_2 moved parallel to itself, toward the NE, at 4.67 m s^{-1} and normal to itself,

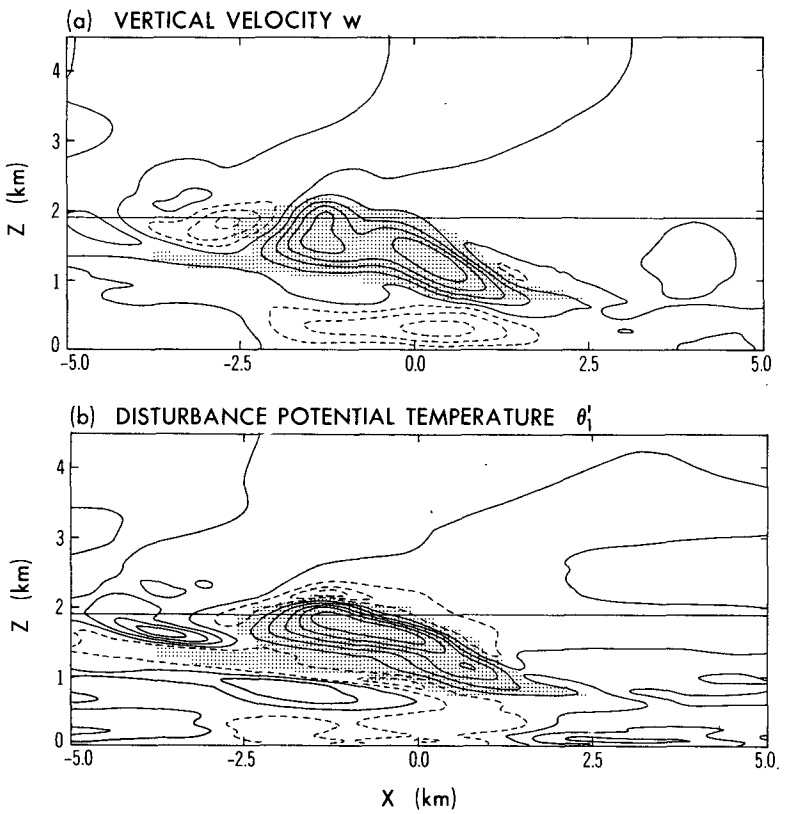

FIG. 5. Vertical x–z cross sections at 80 min for run B_2 at $y = -1.125$ km. (a) Vertical velocity with $w_{max} = 1.34$ m s^{-1} and $w_{min} = -0.91$ m s^{-1}. (b) Disturbance potential temperature θ'. Here $\theta'_{max} = 0.59$ K and $\theta'_{min} = -0.43$ K. Stippled areas represent cloud. Dashed lines indicate negative values. Solid line at $z = 1.906$ km indicates intersection with Fig. 4.

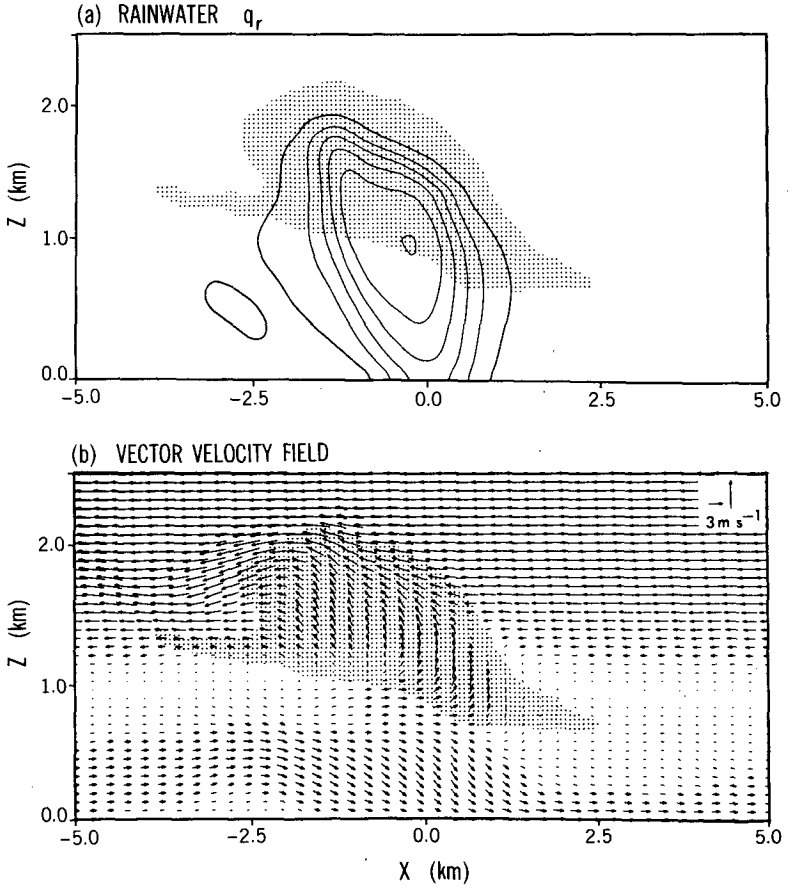

FIG. 6. Vertical x–z cross sections at 80 min for run B_2 at $y = -1.125$ km. Vertical scale is twice the horizontal. (a) Rain water q_r. Maximum value is 0.14 g kg^{-1}. (b) Vector velocity field, relative to model coordinate system, in the x–z plane. Scale for vector velocity is shown in upper right hand corner. Stippled areas represent cloud.

toward the NW, at 0.83 m s^{-1}. In Fig. 7, the base state horizontal velocity profiles are plotted in a coordinate system for which the x'-axis is oriented along the model line of convection, positive toward the NE. As seen in this figure, the forward speed of the line corresponds to a value of U' slightly above cloud base. The air below cloud base has a speed of approximately 0.6 m s^{-1} faster than the movement of the line toward the NE. Thus the boundary layer air is flowing through the line from SW to NE, which is consistent with the analysis of M. LeMone (personal communication). This result is also consistent with the vector velocity field shown in Fig. 6b, where a persistent northward flow pattern is seen below cloud base. The normal velocity of 0.83 m s^{-1} for the line of convection appears to be very close to the mean V'-velocity throughout the cloud and subcloud layers as shown in Fig. 7. It is interesting to note that for this orientation of the (x', y')-coordinates, there is very little organized vertical wind shear in the V'-velocity.

Since it is tedious to obtain flow fields perpendicular to the line axis, y–z cross sections are shown in Fig. 8 for $x = 0.125$ km at 80 min. The variables plotted are the rain water q_r, the vector velocity in the y–z plane and the vertical velocity w. As in Fig. 6, the vertical scale is twice the horizontal. Again, well-organized sinking motion associated with negative buoyancy is present below cloud base and a strong outflow is seen at the surface. An analysis of data from run B_2 indicates that this negative buoyancy is due primarily to evaporative cooling and secondarily to rain water drag. From Fig. 8b the flow of moisture into the cloud seems to be mainly from levels in the upper half of the subcloud layer; however, Fig. 8c shows a slanting channel of positive vertical velocity to the right of the cloud, extending from cloud base to the surface. This pattern appears to be associated with a weak gust front at the surface to the right of the cloud. Thus the flow of at least some surface moisture into the cloud seems likely.

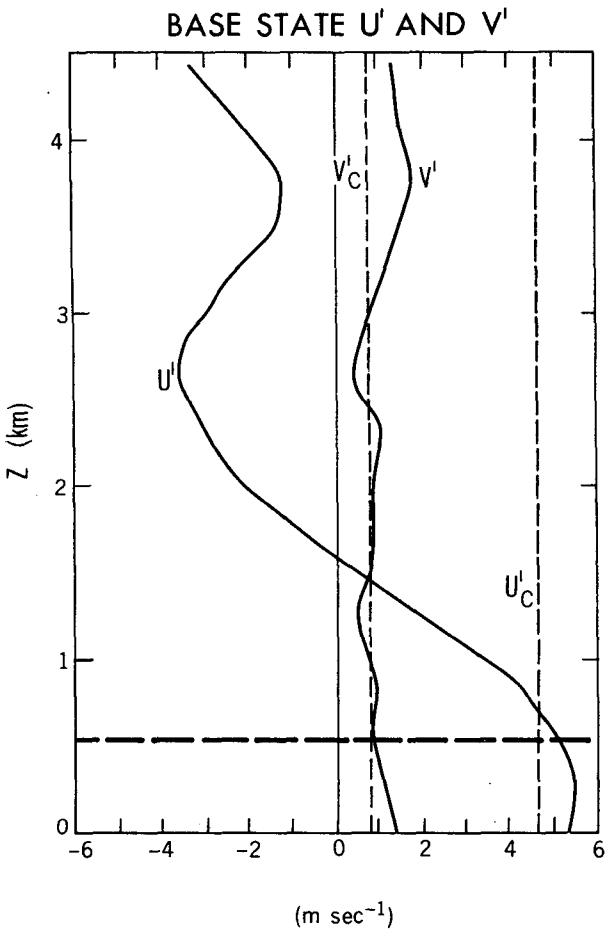

FIG. 7. Initial base state horizontal velocities U' and V' calculated for the x'-axis oriented along the model line of convection in run B_2. Present x'-axis is at an angle of 36.9 deg from N. Dashed lines represent motion of line parallel to itself, U'_c, and normal to itself, V'_c. Heavy dashed line is cloud base.

2) RUN B_3

Vertical cross sections in the x–z plane at $y = -1.125$ km are shown in Fig. 9 for run B_3 at 80 min. In both Figs. 9 and 10, the vertical scale is twice the horizontal. An extensive cloudy area is seen in Fig. 9 with a strong inflow from below cloud base. The strong downward motion in the upper levels is associated with a nearby lateral cloud boundary and strong evaporative cooling. The most significant difference, however, between runs B_2 and B_3 is the flow below cloud base. Evidently, the upward motion below cloud base seen in run B_3 is inhibited in run B_2 by the negative buoyancy due to rain water evaporation. As shown in Fig. 9a, the surface winds are weak below the main cloud base and the leading edge of the convection in Run B_3. This is in contrast to the strong surface winds in run B_2 (shown in Fig. 6) and seen in the observations of Pennell (1975). Thus, although the convection is stronger in

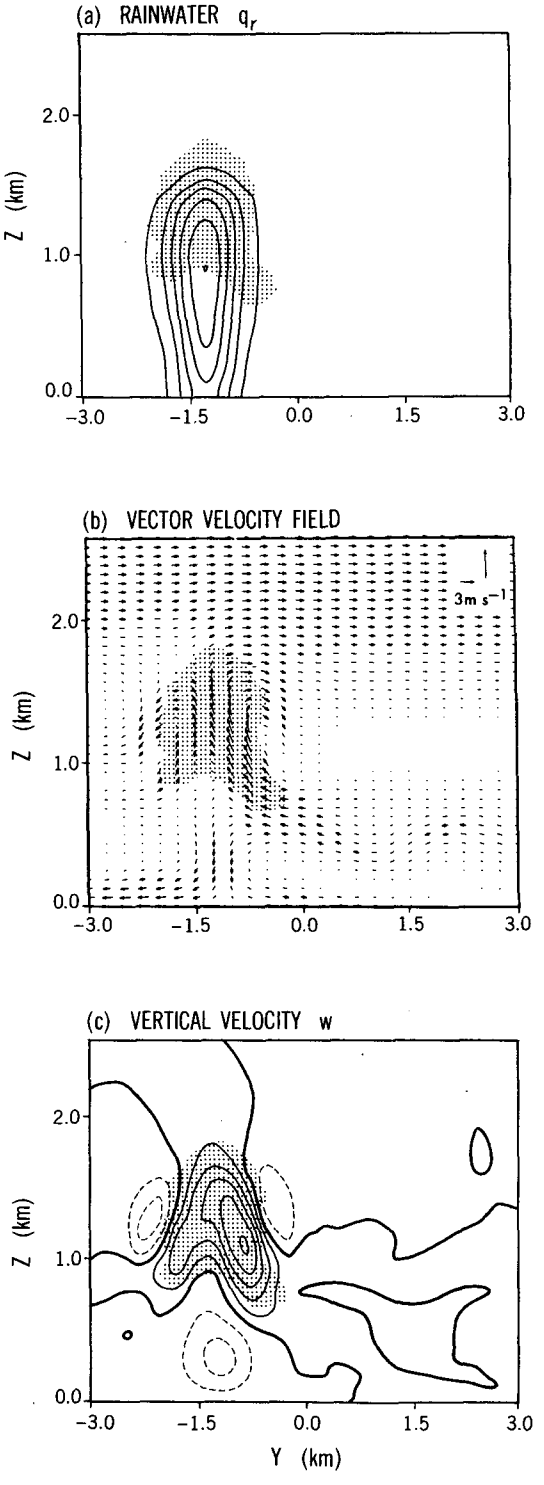

FIG. 8. Vertical y–z cross sections at 80 min for run B_2 at $x = 0.125$ km. Vertical scale is twice the horizontal. (a) Rain water q_r. Maximum value is 0.13 g kg^{-1}. (b) Vector velocity field in the y–z plane. Scale for vector velocity is shown in upper right hand corner. (c) Vertical velocity with $w_{max} = 1.70$ m s^{-1} and $w_{min} = -0.82$ m s^{-1}. Heavy lines are the zero contours. Dashed lines indicate negative values. Stippled areas represent cloud.

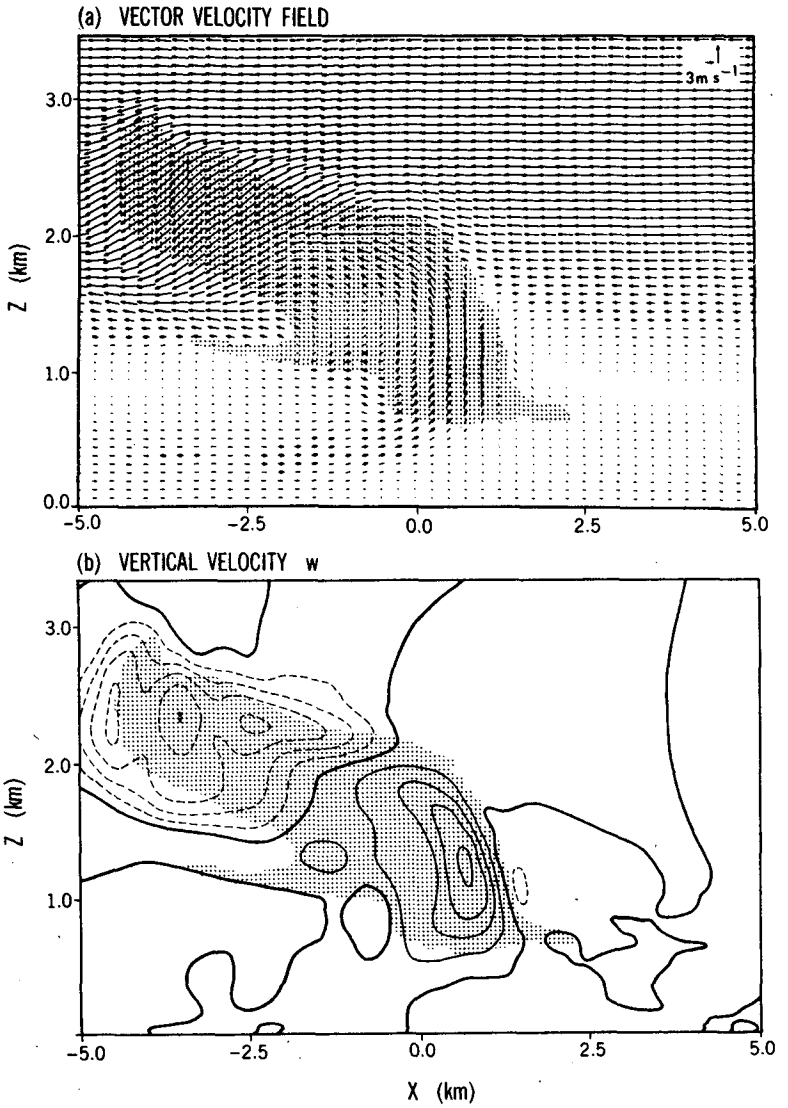

FIG. 9. Vertical x–z cross sections at 80 min for run B_3 at $y = -1.125$ km. Vertical scale is twice the horizontal. (a) Vector velocity field, relative to model coordinate system, in the x–z plane. Scale for vector velocity is shown in upper right-hand corner. (b) Vertical velocity with $w_{max} = 2.57$ and $w_{min} = -3.05$ m s^{-1}. Heavy lines are the zero contours. Dashed lines indicate negative values. Stippled areas represent cloud.

run B_3, the flow near the surface is not realistic, indicating the importance of the rain phase in the observed convection.

In Fig. 10, vertical cross sections are shown in the y–z plane at $x = 0.125$ km for run B_3 at 80 min. This figure can be compared with Fig. 8 for run B_2. The most significant difference in the flow fields is again the downdraft below cloud base and the resulting surface outflow in run B_2. As a consequence, for run B_3, more moisture enters the cloud from below cloud base and less from the current to the right of the cloud. Except for run B_3 being stronger, other aspects of the flow are relatively similar. Note that for both runs B_2 and B_3 downdrafts develop on the lateral cloud boundaries in middle to upper cloud levels.

6. Discussion of the remaining calculations

A comparison of the curves for θ_0 and θ_{moist} in Fig. 1a indicates that the present sounding has the potential for strong moist instability. The two-dimensional calculations examine the role of the vertical wind shear shown in Fig. 1b for determining the strength of the convection. In run A_1, with the flow independent of

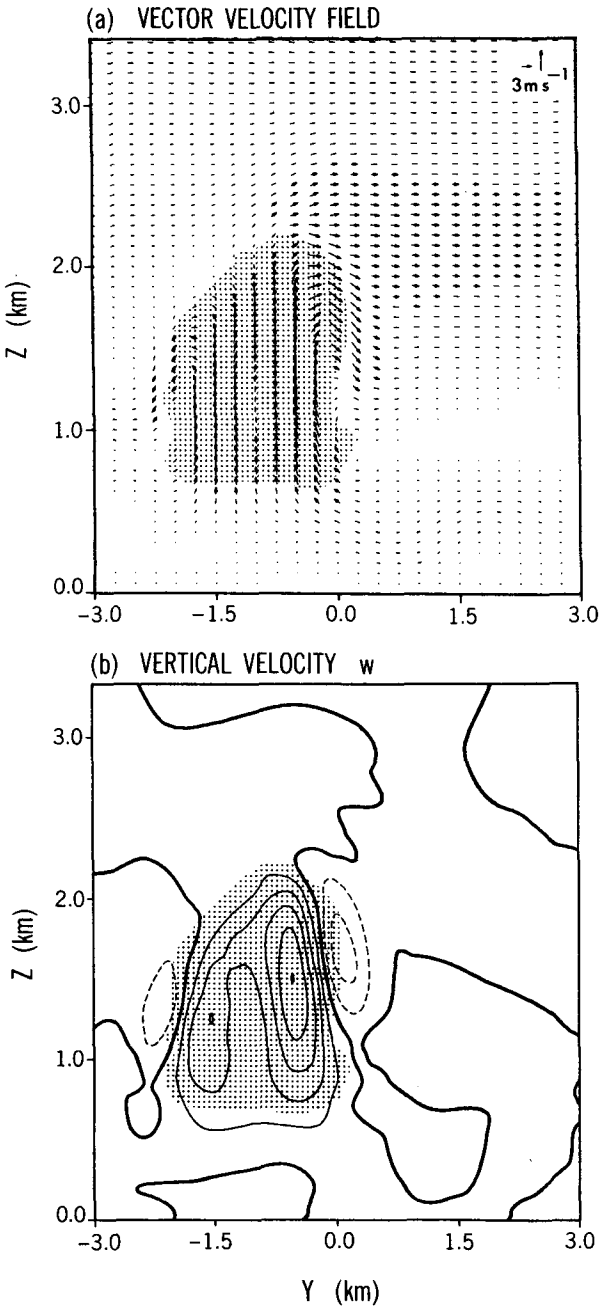

FIG. 10. Vertical y–z cross sections at 80 min for run B_3 at x = 0.125 km. Vertical scale is twice the horizontal. (a) Vector velocity field in the y–z plane. Scale for vector velocity is shown in upper right-hand corner. (b) Vertical velocity with w_{max} = 3.79 and w_{min} = −1.67 m s^{-1}. Heavy lines are the zero contours. Dashed lines indicate negative values. Stippled areas represent cloud.

y, the strong shear in the base state U-velocity has an inhibiting effect upon the growth of the convection. For this calculation the convection is weaker than in run B_2. Only two isolated cells developed at 45 and 80 min. For both of these cells the cloud tops reached 2.7 km. In run A_2, with the flow independent of x, the vertical wind shear in the base state V-velocity is much weaker and the resulting convection is much stronger. The initial cell kept growing until the cloud top reached 4.3 km at 50 min. The maximum vertical velocity was 4.5 m s^{-1}. In contrast, the maximum vertical velocity in run A_1 was less than 3 m s^{-1}.

In run C_1 the Newtonian damping term $-D_i$ has been set equal to zero in the momentum equation (2.5). The variation of w_{max} with time for runs C_1 and B_2 is shown in Fig. 11. These two calculations are nearly identical at early times, but by 45 min and later w_{max} becomes progressively larger for run C_1. Evidently, relaxing the restraint on the horizontal velocities due to the $-D_i$ term in Eq. (2.5) allows stronger convection after sufficient time in run C_1.

Dropping the newtonian damping term $-D_i$ has the most noticeable effect upon the mean flow at low levels. In Fig. 12 the horizontal mean $\langle u_T \rangle$, which includes the 4 m s^{-1} translation speed of the model coordinates, has been plotted for runs C_1 and B_2 at 80 min for $0 \leq z \leq 1.0$ km. Also shown is the initial base state U-velocity. Relative to the initial U-velocity, the deviations of $\langle u_T \rangle$ for both calculations are in the same sense but, as expected, the variation is larger in run C_1 where the $-D_i$ term has been dropped from Eq. (2.5).

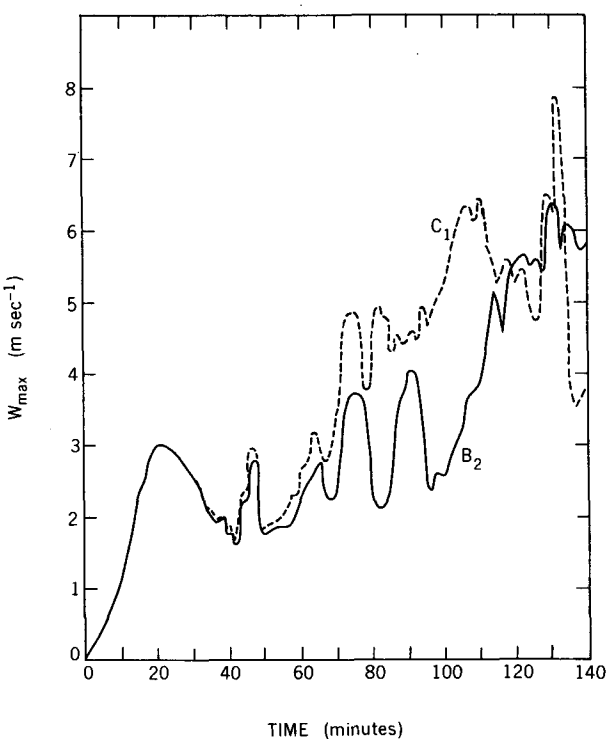

FIG. 11. Plot of maximum vertical velocity w_{max} with time. Solid line, run B_2; short-dashed line, run C_1.

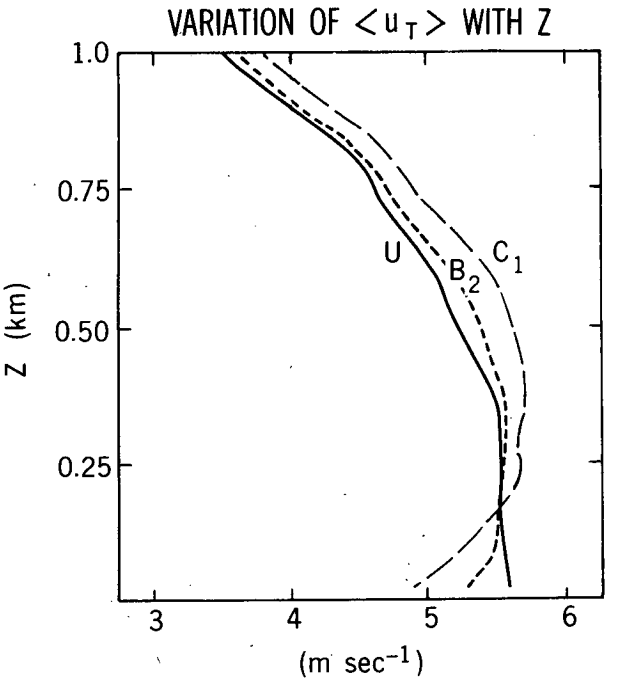

FIG. 12. Horizontal average $\langle u_T \rangle$ at 80 min for $0 \leq z \leq 1.0$ km. Solid line, base state U-velocity; short-dashed line, run B_2; long-dashed line, run C_1.

Below 180 m, the flow speed is reduced with a significant reduction in $\langle u_T \rangle$ for run C_1 at the surface.

Other calculations which result in significant changes in the surface $\langle u_T \rangle$ with time have been carried out. All of these calculations indicate stronger convection when the surface $\langle u_T \rangle$ is reduced. Thus, we infer that the reduction in the surface $\langle u_T \rangle$ in run C_1 is probably related to the stronger convection in that run. This large reduction in $\langle u_T \rangle$ may be unrealistic; it appears that the surface stress terms are not being properly balanced by other physical effects in the model. As a consequence, the stronger growth in run C_1 may also be unrealistic. Thus, while we consider the incorporation of the $-D_i$ term in Eq. (2.5) an undesirable feature of the present model, run C_1, in which it is eliminated, is not necessarily a more realistic simulation for the present calculations. More recent simulations of tropical maritime convection have eliminated both the $-D_i$ term in Eq. (2.5) and the surface stress terms.

The final two calculations in Table 1 are run C_2, which does not have the 5% moisture augmentation shown in Fig. 1a, and run C_3, which has periodic lateral boundary conditions in y. The plot of w_{max} versus time for runs C_2, C_3, and B_2 is shown in Fig. 13. In run C_2 only two primary cells developed, the first cell just after 20 min due to the initial disturbance and a later cell at 130 min. The initial cell is somewhat stronger than it was for run B_2 because the virtual temperature difference between the cell and its environment is stronger for run C_2. This is a result of less moisture in the environment as the cell rises. The second cell at 130 min had a cloud top of 2.6 km and $w_{max} = 4.3$ m s^{-1}. Note that in run B_2 at 130 min the convection was approaching the upper boundary. Finally, in run C_3 the convection was weak. Only three cells developed in 140 min with the highest cloud top at 2.3 km and $w_{max} = 2.9$ m s^{-1}.

Since the purpose of run C_3 was to simulate a line of convection oriented NW to SE as reported by Pennell (1975), this calculation has been unsuccessful in this goal. Evidently, the periodic boundary conditions inhibited the flow of moisture across the lateral boundaries into the convective cells as is possible with open boundary conditions. In contrast, it will be shown below that run B_2 represents a good simulation of a "finger" of convection which developed perpendicular to the line observed by Pennell.

7. Comparisons with observations

In Fig. 14 the GATE radar hourly rainfall between 1400 and 1500 UTC on day 226 is shown. Each entry represents rainfall data for a 4 km × 4 km square. The total figure is an 80 km × 80 km square and thus has 20 entry squares on a side. This figure represents a small subsection of the standard plot of GATE radar hourly rainfall. The 9°00′ N lat and 24°20′ W long lines give a point of reference for the present data. Also, the research ship *Gillis* (9°15′ N, 24°48′ W) is approximately 36 km to the west of the western boundary of the present figure. The code for rainfall amounts is given at the top of the figure.

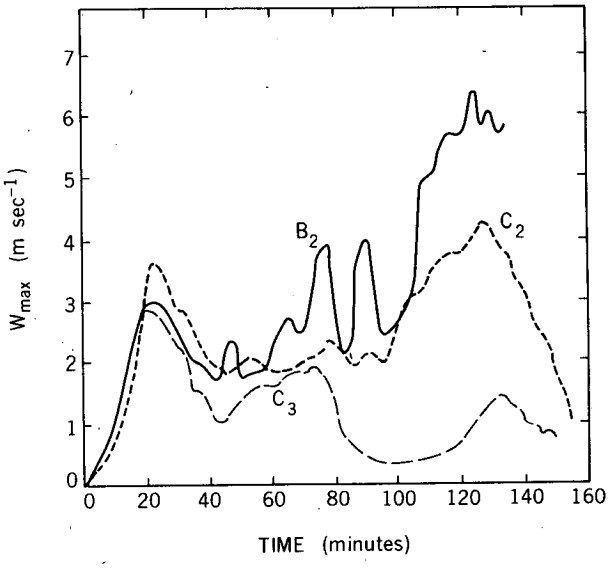

FIG. 13. Plot of maximum vertical velocity w_{ax} with time. Solid line, run B_2; short-dashed line, run C_2; long-dashed line run C_3.

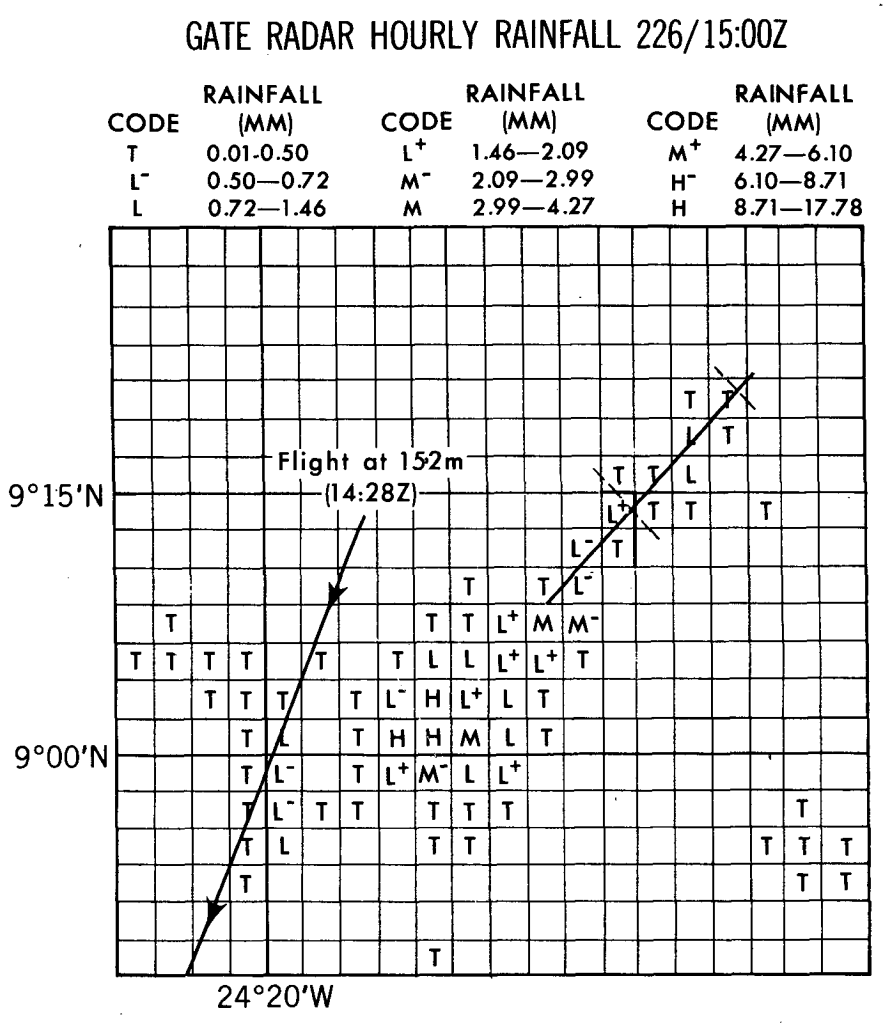

FIG. 14. The GATE radar hourly rainfall between 1400 and 1500 UTC on day 226. Code for precipitation amounts is given at top of figure. Each entry represents data for a 4 km × 4 km square. Line with arrows indicates flight path at 152 m which started at 1428 UTC. Line NE–SW through light precipitation is compared with data from run B_2. See discussion in text.

The line with arrows on it indicates the path of the flight starting at 1428 UTC discussed by Pennell (1975). The wind data at z = 152 m from this flight are shown in his Fig. 2. Also, there is reasonable correspondence between the radar echoes shown in his figure and the rainfall amounts shown in Fig. 14 near this line. This flight track was used to determine the x-axis in the present model simulations.

The line oriented NE–SW in the northeastern quadrant of Fig. 14 is the observed line which is compared with run B_2 in the present study. The perpendicular dashed lines indicate the length of growth of this line between 1400 and 1500 UTC. The right angle solid line between entry points indicates the northeastern most extension of this line at 1400 UTC. Using a higher resolution section of this area of Fig. 14, we find that the observed line has an angle of 42.4 deg with respect to North. Between 1400 and 1500 UTC the line developed to the NE, parallel to itself, at 4.58 m s^{-1}. The perpendicular motion of the line during this hour appears to be very small; a value of zero has been entered in Table 2. The final point to note about Fig. 14 is that there is moderate to heavy precipitation to the southwest of this line. As noted earlier, the simulation of this area of precipitation is beyond the scope of the present study.

A detailed comparison of the data for the line in run B_2 and the observed line shown in Fig. 14 is given in Table 2. Good agreement is seen between the two lines for line orientation, line speed and cloud top height.[1]

[1] It is assumed that Pennell's observations for cloud top and cloud base also apply to the line in the NE quadrant of Fig. 14.

TABLE 2. Comparison of run B_2 with observed line.

Parameter	Run B_2	Observed line
Line orientation (deg True)	36.9	42.4
Line speed (m s^{-1})		
parallel to line	4.67	4.58
normal to line	0.83	0
Width of line (km)	1.5	2–4 ?*
cloud base (km)	0.562	0.400
cloud top (km)	3.0	3.0
Precipitation (cm h^{-1})	0.01–0.02	0.07–0.15

* See text for explanation of question mark.

The difference in the line orientations with respect to North is only 5.5 deg. The line speed, parallel to itself, is nearly the same for both lines. Also both lines show little or no normal motion. Due to the crude nature of the calculation of the observed line speed, this agreement for line speeds may be somewhat fortuitous. Cloud tops are at 3.0 km for both run B_2 and the line discussed by Pennell (1975).

The apparent agreement of the line width in run B_2 with observations is not as good, although a fully definitive comparison is not possible as will be explained below. The value of 1.5 km for the line width in run B_2 was obtained from the width of the cloud normal to the line at $z = 1.031$ km at 80 min. The width of the simulated line is obviously dependent on the initial disturbance, but seems reasonable in comparison with the depth of individual clouds. The width of 2–4 km for the observed line was estimated from Fig. 14, noting that each entry for precipitation represents a 4 km × 4 km square. This estimated width, however, may be exaggerated because each square represents a full hour for the radar rainfall. For example, even a small normal velocity of the line would add a significant apparent broadening of the line width. For this reason a question mark is placed after this entry in Table 2.

Poor agreement is seen in Table 2 for the cloud base height and precipitation. M. LeMone (personal communication) has suggested that the simulated cloud base is higher than the 400 m observed by Pennell (1975) because the actual sounding is cooler and more moist at low levels than that shown in Fig. 1a. Indeed, for our initial sounding, a simple parcel calculation indicates that air starting from either the surface or midsubcloud levels will first condense near the cloud base level in run B_2. We had initially thought that the higher cloud base in run B_2 could be related to the relatively horizontal trajectories of the flow entering the cloud base as seen in Figs. 6 and 8. The parcel calculation, however, does not give support to this speculation. Furthermore, in run B_3, where the cloud roots penetrate deeper into the subcloud layer, the cloud base is effectively at the same level as in run B_2. Thus it appears that our initial sounding is compatible with a cloud base near 550 m rather than 400 m as observed.

Finally, the maximum precipitation at the ground was only 0.01–0.02 cm in run B_2, compared with 0.07–0.15 cm for the observed line. If the sounding below cloud base was too warm and dry in run B_2, this could result in less condensation in the cloud and hence a smaller amount of precipitation reaching the ground. The value of precipitation for the observed line in Fig. 14 was taken from that portion of the line which formed between 1400 and 1500 UTC.

8. Summary

Pennell (1975) reported that on day 226 of GATE the line of convection was oriented in a northwest to southeast direction and ran from *Oceanographer* to *Gillis* and beyond. This orientation is evidently the large-scale organization of the line, especially early in the day. The present simulations were not able to reproduce the line with this orientation, but rather simulated a northeastward propagating "finger" of convection which was in reasonable agreement with radar data at 1500 UTC.

The primary calculation, run B_2, was in excellent agreement with the observed line shown in Fig. 14 for its orientation and its propagation speed toward the northeast; in poorer agreement, the cloud base was too high and the precipitation was weak. The latter two features of run B_2 appear to be associated with a base state sounding which is too warm and too dry below cloud base.

The simulated convection was sensitive to the value of $\rho_0 q_{cm}$, which is the onset value for the autoconversion of cloud water into rain water. The strongest convection occurred for run B_3 in which no rain water formed. This calculation, however, was unrealistic with weak horizontal flow at the surface. In run B_2, strong cooling due to evaporation of rain water took place below cloud base. As a result, the weaker branch of the horizontal flow in the x–z plane entered the sloping cloud base and the stronger branch descended toward the surface (Fig. 6). The strong horizontal flow at the surface and the well-defined leading edge of the convection are in good agreement with the observations of Pennell (1975).

Some other features of the convection in run B_2 are worthy of noting. In Fig. 7, with the x'-axis parallel to the line, the base state U'-velocity below cloud base appears to move through the line from SW to NE. With this orientation, the base state V'-velocity has little organized wind shear. Also, the line moves normal to itself toward the NW with the mean V'-velocity in the cloud and subcloud layers. Finally, Figs. 6 and 8 suggest that the primary source of moisture for the cloud is the upper half of the subcloud layer, with nearly horizontal flow entering the cloud.

In conclusion, a word of caution must be made in the comparison of run B_2 with the observed data. It should be remembered that the base state moisture distribution had a 5% augmentation over the observed values as shown in Fig. 1a for vertical levels between $z = 0.7$ and 2.0 km. When this calculation was performed without the moisture augmentation (run C_2), the convection was too weak as shown in Fig. 13. Thus, while the results of the present simulation are promising, they only represent a beginning to an understanding of the observed shallow convection.

Acknowledgments. Our thanks go to Issac Held and Yoshio Kurihara of the Geophysical Fluid Dynamics Laboratory for reading the manuscript and making many helpful suggestions. The authors have also benefited significantly from discussions with Peggy LeMone of NCAR concerning this work. The calculations were carried out on the CYBER computers at GFDL. The figures were drafted by Philip G. Tunison and staff, and the manuscript typed by Wendy Marshall.

APPENDIX

Subgrid-Scale Turbulence Parameterization

The present scheme to represent subgrid-scale mixing differs from that in LH82 and LH86 in two respects. First, the vertical mixing is greatly reduced in regions with stable stratification. This is accomplished through the development of a generalized criterion of vertical static stability, which applies both in and out of clouds. A preliminary version of this scheme was given in LH86 where vertical mixing was reduced in clear air with stable stratification. Secondly, the present scheme has been modified so that reasonable values of mixing occur when Δx, Δy and Δz differ significantly in size.

1. Criterion for vertical static stability

Before discussing the vertical static stability, it is appropriate to give the form of the eddy viscosity K_m which is evaluated at w-grid points. The most general expression for K_m includes both deformation and unstable stratification effects (Lilly 1962; Clark 1979). Although different in appearance, the expression below for K_m can be shown to be equivalent to that given by (A22) in LH82:

$$K_m = c^2\Delta^2\left\{\frac{D^2}{2} - \frac{2}{3}\left(\frac{\partial u_k}{\partial x_k}\right)^2 - 3\delta g\frac{\partial B_T}{\partial z}\right\}^{1/2}, \quad \text{(A1)}$$

where $c = 0.21$, $\Delta = (\Delta x\Delta y\Delta z)^{1/3}$ and $\delta = 0$, 1; if $\partial B_T/\partial z \geq 0$, $\delta = 0$; if $\partial B_T/\partial z < 0$, $\delta = 1$. The factor of 3, multiplying δ, represents the ratio K_h/K_m as given by Deardorff (1972). In addition, we have defined the following:

$$D^2 = \left(\frac{\partial u_i}{\partial x_j} + \frac{\partial u_j}{\partial x_i}\right)\left(\frac{\partial u_i}{\partial x_j} + \frac{\partial u_j}{\partial x_i}\right), \quad \text{(A2)}$$

$$\frac{\partial B_T}{\partial z} = \frac{1}{\theta_0}\frac{\partial}{\partial z}(\theta_0 + \theta_1) + 0.608\frac{\partial q_v}{\partial z} - \frac{\partial q_c}{\partial z} - \frac{\partial q_r}{\partial z} + \frac{f}{(1+\beta\gamma)}\left(\frac{\gamma}{\theta_0} - 0.608\right)\left[\frac{\partial q_v}{\partial z} - \beta\frac{\partial}{\partial z}(\theta_0 + \theta_1)\right], \quad \text{(A3)}$$

$$\left.\begin{aligned}\beta &= \frac{Lq_{vs}(1 + 1.608q_{vs})}{R_v T_0\theta_0}\\ \gamma &= \frac{L}{c_p\pi_0}\end{aligned}\right\}, \quad \text{(A4)}$$

where it is seen that β, γ and D^2 are defined as in LH82. It is important to remember that K_m is evaluated at w-grid points which are staggered in the vertical with q_c-grid points. Thus f is the same parameter as defined in Lipps (1977) with its value determined by whether cloud water exists directly above and/or below the K_m-grid point. Hence $f = 1$ inside of clouds, 0 outside of clouds, and 0.5 on a cloud edge.

From Eqs. (A1) and (A3) it is seen that $\partial B_T/\partial z$ is a generalized measure of static stability. The first two terms on the right-hand side of (A3) give the vertical gradient of virtual potential temperature θ_v divided by θ_0. The next two terms represent the effect of liquid water drag and the final term multiplied by f represents the effect of condensation on the moist static stability.

Thus, it is $\partial B_T/\partial z$ which is used to determine the vertical stability of the atmosphere. First, we define a local Richardson number:

$$\mathrm{Ri} = g\frac{\partial B_T}{\partial z}\left\{\frac{D^2}{2} - \frac{2}{3}\left(\frac{\partial u_k}{\partial x_k}\right)^2\right\}^{-1}. \quad \text{(A5)}$$

Furthermore, when the denominator

$$\frac{D^2}{2} - \frac{2}{3}\left(\frac{\partial u_k}{\partial x_k}\right)^2 = 0,$$

it is set equal to 10^{-10}. Finally, we define the factor which will multiply either K_m or K_h for cases of vertical mixing:

$$S = \frac{1}{1 + 10\,\mathrm{Ri}}, \quad \mathrm{Ri} \geq 0 \quad \text{(stable)} \quad \text{(A6a)}$$

$$S = 1, \quad \mathrm{Ri} < 0 \quad \text{(unstable)}. \quad \text{(A6b)}$$

In addition, a limit is placed on S so that $S \geq 10^{-2}$.

2. Expressions for subgrid-scale fluxes

The present expressions for subgrid-scale fluxes are modified from those given in LH82 by the parameter S and by taking account of the variations in the magnitudes of Δx, Δy and Δz. The parameter S is analogous to F given in the appendix of LH86. The components of the Reynolds stress τ_{ij} are given by

$$\left.\begin{aligned}
\tau_{11} &= \rho_0 K_m\left[2\left(\frac{\partial u}{\partial x}\right)\left(\frac{\Delta x}{\Delta}\right)^2 - \frac{2}{3}DIVM\right]\\
\tau_{22} &= \rho_0 K_m\left[2\left(\frac{\partial v}{\partial y}\right)\left(\frac{\Delta y}{\Delta}\right)^2 - \frac{2}{3}DIVM\right]\\
\tau_{33} &= \rho_0 K_m\left[2\left(\frac{\partial w}{\partial z}\right)\left(\frac{\Delta z}{\Delta}\right)^2 - \frac{2}{3}DIVM\right]\\
\tau_{12} &= \tau_{21} = \rho_0 K_m\left[\frac{\partial u}{\partial y}\left(\frac{\Delta y}{\Delta}\right)^2 + \frac{\partial v}{\partial x}\left(\frac{\Delta x}{\Delta}\right)^2\right]\\
\tau_{13} &= \tau_{31} = \rho_0 S K_m\left[\frac{\partial u}{\partial z}\left(\frac{\Delta z}{\Delta}\right)^2 + \frac{\partial w}{\partial x}\left(\frac{\Delta x}{\Delta}\right)^2\right]\\
\tau_{23} &= \tau_{32} = \rho_0 S K_m\left[\frac{\partial v}{\partial z}\left(\frac{\Delta z}{\Delta}\right)^2 + \frac{\partial w}{\partial y}\left(\frac{\Delta y}{\Delta}\right)^2\right]
\end{aligned}\right\} \quad \text{(A7)}$$

where $DIVM$ is defined by

$$DIVM = \frac{\partial u}{\partial x}\left(\frac{\Delta x}{\Delta}\right)^2 + \frac{\partial v}{\partial y}\left(\frac{\Delta y}{\Delta}\right)^2 + \frac{\partial w}{\partial z}\left(\frac{\Delta z}{\Delta}\right)^2. \quad \text{(A8)}$$

Thus the trace τ_{kk} of the Reynolds stress tensor τ_{ij} vanishes. In terms of the upper and lower boundary conditions discussed in section 2.c, it is relevant to note that $\tau_{13} = -\rho_0\overline{u'w'}$ and $\tau_{23} = -\rho_0\overline{v'w'}$.

The vertical subgrid-scale fluxes of θ, q_v, q_c and q_r are given by

$$-\rho_0\overline{w'\theta'} = \rho_0 S K_h\left[\frac{\partial}{\partial z}(\theta_0 + \theta_1) + \frac{f\gamma}{(1+\beta\gamma)}\left(\frac{\partial q_v}{\partial z} - \beta\frac{\partial}{\partial z}(\theta_0 + \theta_1)\right)\right]\left(\frac{\Delta z}{\Delta}\right)^2 \quad \text{(A9)}$$

$$-\rho_0\overline{w'q_v'} = \rho_0 S K_h\left[\frac{\partial q_v}{\partial z} - \frac{f}{(1+\beta\gamma)} \times\left(\frac{\partial q_v}{\partial z} - \beta\frac{\partial}{\partial z}(\theta_0 + \theta_1)\right)\right]\left(\frac{\Delta z}{\Delta}\right)^2 \quad \text{(A10)}$$

$$-\rho_0\overline{w'q_c'} = \rho_0 K_h\frac{\partial q_c}{\partial z}\left(\frac{\Delta z}{\Delta}\right)^2 \quad \text{(A11)}$$

$$-\rho_0\overline{w'q_r'} = \rho_0 K_h\frac{\partial q_r}{\partial z}\left(\frac{\Delta z}{\Delta}\right)^2. \quad \text{(A12)}$$

As indicated above, the coefficient of eddy diffusivity K_h is given by $K_h = 3K_m$ (Deardorff 1972). Apart from the multiplication factor $S(\Delta z/\Delta)^2$, the subgrid-scale fluxes $\rho_0\overline{w'\theta'}$ and $\rho_0\overline{w'q_v}$ are specified the same as in LH82.

The horizontal fluxes of the above variables can be represented by the compressed notation

$$-\rho_0\overline{u's'} = \rho_0 K_h\frac{\partial s}{\partial x}\left(\frac{\Delta x}{\Delta}\right)^2 \quad \text{(A13)}$$

$$-\rho_0\overline{v's'} = \rho_0 K_h\frac{\partial s}{\partial y}\left(\frac{\Delta y}{\Delta}\right)^2 \quad \text{(A14)}$$

where s is a generalized variable which represents either θ, q_v, q_c or q_r. As noted in LH82, this simplified form applies to the horizontal fluxes of θ and q_v since the terms involving condensation effects, which are multiplied by f in (A9) and (A10), vanish for the horizontal subgrid-scale fluxes.

Note that the vertical mixing of cloud water q_c and rain water q_r is not reduced by the factor S for stable conditions. In retrospect, it is now considered an oversight that this factor was not used for these variables as well. Thus in future calculations the S factor will be included for the vertical mixing of q_c and q_r.

REFERENCES

Clark, T. L., 1979: Numerical simulations with a three-dimensional cloud model: Lateral boundary condition experiments and multicellular severe storm simulations. *J. Atmos. Sci.*, **36**, 2191–2215.

Crowley, W. P., 1968: Numerical advection experiments. *Mon. Wea. Rev.*, **96**, 1–11.

Deardoff, J. W., 1972: Numerical investigation of neutral and unstable planetary boundary layers. *J. Atmos. Sci.*, **29**, 91–115.

Kessler, E., 1969: On the distribution and continuity of water substance in atmospheric circulations. *Meteor. Monogr.* No. 32, Amer. Meteor. Soc., 84 pp.

Klemp, J. B., and R. Wilhelmson, 1978: The simulation of three-dimensional convective storm dynamics. *J. Atmos. Sci.*, **35**, 1070–1096.

Lilly, D. K., 1962: On the numerical simulation of buoyant convection. *Tellus*, **14**, 148–172.

Lipps, F. B., 1977: A study of turbulence parameterization in a cloud model. *J. Atmos. Sci.*, **34**, 1751–1772.

——, and R. S. Hemler, 1982: A scale analysis of deep moist convection and some related numerical calculations. *J. Atmos. Sci.*, **39**, 2192–2210.

——, and ——, 1986: Numerical simulation of deep tropical convection associated with large-scale convergence. *J. Atmos. Sci.*, **43**, 1796–1816.

Malkus, J. S., 1954: Some results of a trade-cumulus cloud investigation. *J. Meteorol.*, **11**, 220–237.

Manton, M. J., and W. R. Cotton, 1977: Formulation of approximate equations for modeling deep moist convection on the mesoscale. Atmos. Sci. Paper No. 266, Colorado State University, Fort Collins, CO 80523.

Ogura, Y., and N. A. Phillips, 1962: Scale analysis of deep and shallow convection in the atmosphere. *J. Atmos. Sci.*, **19**, 173–179.

Orlanski, I., 1976: A simple boundary condition for unbounded hyberbolic flows. *J. Comput. Phys.*, **21**, 251–269.

Pennell, W. T., 1975: A study of the subcloud layer in the vicinity of an isolated line of cumulus. GATE Report 14 Prelim. Sci. Results, (Vol. 1), of the GARP Atlantic Trop. Experiment. Published by the ICSU, WMO, 276–286, NTIS No.-N75-27466.

Silverman, B. A., and D. A. Mathews: *Appendix D of Weather Modification Research Programme: International Cloud Modelling Workshop/Conference.* WMO, Geneva, Sept. 1986, WMO/TD-No. 139.

Tripoli, G. J., and W. R. Cotton, 1980: A numerical investigation of several factors contributing to the observed variable intensity of deep convection over South Florida. *J. Appl. Meteorol.*, **19**, 1037–1063.